Proceedings of ASME Turbo Expo 2022
GT2022
June 13-17, 2022, Rotterdam, The Netherlands

GT2022-82149

NUMERICAL INVESTIGATIONS OF THE UNSTEADY AERODYNAMIC CHARACTERISTICS FOR INTAKES AT CROSSWIND

Tommaso Piovesan[1], Zhang Wenqiang[2], Mehdi Vahdati[2], Pavlos K. Zachos[1]

[1]Propulsion Engineering Centre, School of Aerospace, Transport, and Manufacturing
Cranfield University, Bedfordshire, UK
[2]Mechanical Engineering Department, Imperial College London, UK

ABSTRACT

The ground vortex generated in front of an intake operating near the ground and subjected to crosswind is investigated using CFD and compared to the experiments. The flow field of a scale-model intake is numerically simulated with both steady and unsteady approach, with the aim to predict ground vortex effects and to characterize the vortex unsteady behaviour. The experimental results showed that for an intake near the ground under crosswind the ground vortex that forms under the intake and the in-duct separation, when present, exhibit unsteady behaviour that becomes stronger as the crosswind velocity is increased. The simulations indicate that a steady-state approach only partially reproduces the time-averaged ground vortex characteristics and in-duct distortion losses, while an unsteady approach shows a lower level of unsteadiness compared to the experimental observations. The consequences of the unsteady flow in the intake on the fan aerodynamic and aeroelastic stability are finally discussed to reinforce that these can result in significant non-synchronous vibration (NSV) and loss of stall margin which cannot be adequately assessed if no unsteady component of the inlet distortions is taken into account.

Keywords: Ground vortex, unsteady distortion, numerical, forced response.

NOMENCLATURE

A_i	Intake internal cross flow area, m^2
A_∞	Captured stream tube cross flow area, m^2
AIP	Aerodynamic Interference Plane
DC_{60}	Sectional distortion coefficient
D_i	Intake internal diameter, *m*
D_l	Intake highlight diameter, *m*
D_{max}	Maximum intake external diameter, *m*
EO	Engine order
h	Ground clearance, *m*
$P_{0,AIP}$	Area averaged AIP total pressure, *Pa*
$P_{0,\infty}$	Freestream total pressure, *Pa*
r_c	Vortex core radius, *m*
r_i	Intake internal radius, *m*
U_i	Intake centreline velocity, *m/s*
U_∞	Freestream velocity, *m/s*
U^*	Non-dimensional velocity ratio
Γ	Circulation, s/m^2
Γ^*	Non-dimensional circulation
δ^*	Boundary layer thickness, *m*
θ	Azimuthal direction, *deg*
ω_z	Out-of-plane vorticity, s^{-1}

1. INTRODUCTION

One of the most severe off-design operating conditions for an aero-engine is crosswind operation when a vortex can likely develop due to the interaction of the ground and the engine's intake. Under such conditions a separation can occur around the windward lip and a vortex, commonly known as *ground vortex* or *ingested vortex*, can be induced across the intake which can be detrimental to the performance of the downstream fan, or cause ingestion of foreign object debris (FOD) [1], [2]. Moreover, the non-homogeneous flow field upstream of the fan will create asynchronous aerodynamic forcing on the fan which in case of resonance can result in large amplitude vibrations. The ground vortex and the in-duct separation, are intrinsically characterized by unsteadiness, causing the vortex, and the separated region to oscillate in terms of position, size, and intensity. The effects of this unsteadiness on fan stability have

been partially studied before predominantly under the assumption that the inlet distortion had no unsteady component.

Previous studies have been conducted focusing on the ground vortex aerodynamics and the separation effects on intake performance under crosswind conditions. These aspects include for instance formation mechanisms and criteria, vortex unsteadiness and meandering, analysis of the influence of operating conditions and geometric parameters on the ground vortex, or effects on the downstream fan. The vortex formation mechanisms under crosswind were originally investigated experimentally by Siervi et al. [3]. Two different flow topologies were identified, that can be schematically illustrated in Figure 1 and Figure 2. Considering an intake of highlight D_l located at a certain ground clearance (or height-to-diameter ratio h/D_l) and subjected to a crosswind velocity U_∞, the flow field topology around the intake varies according to h/D_l and the intake-to-wind velocity ratio U_i/U_∞, where U_i indicates the intake velocity and U_∞ corresponds to the cross-wind velocity. For an incompressible flow, the operating velocity ratio $U^* = U_i/U_\infty$ corresponds to the flow area ratio A_∞/A_i (or mass flow capture ratio), which provides a measure of the mass flow captured by the engine stream-tube. For high values of h/D_l or low values of U_i/U_∞, that is for low values of mass flow, the capture stream-tube does not interact with the ground plane and two counter rotating vortices form off the leeward lip of the intake (see Figure 1). On the contrary, for low values of h/D_l or high values of U_i/U_∞, that is when the intake is operating closer to the ground or at higher values of mass flow, the stream-tube interacts with the ground and a single vortex forms under the intake, while a single trailing vortex is present off the leeward lip (Figure 2). Different correlations relating the vortex formation to the height-to-diameter ratio of the intake and the velocity ratio, which is linked to the size of the capture stream-tube were presented in previous experimental or numerical studies ([4], [5], [6], [7] [8]). The dependency of the formation of the ground vortex from h/D_l and U_i/U_∞ and its strength were illustrated graphically or modelled mathematically in terms of vortex formation maps, which estimate the threshold for the insurgence of the vortex and predict its strength based on qualitative visualizations and/or quantitative measurements and simulations. Murphy et al. [9] performed an extensive experimental study to investigate ground vortex formation mechanisms for an aspirated intake operating in crosswind by means of Stereoscopic Particle Image Velocimetry (SPIV). A quantitative analysis of the effects of different parameters, such as crosswind velocity, ground clearance, and approaching boundary-layer thickness was carried out, identifying the vortex characteristics in terms of intensity and radius to be highly dependent on the velocity ratio, crosswind velocity, and the distance of the intake from the ground. The unsteady characteristics of the ground vortices were also investigated, observing variations of the vortex core radius and position with time. The vortex tends to move in front of the intake in the direction of the crosswind and the amplitude of this movement was found to increase with crosswind velocity.

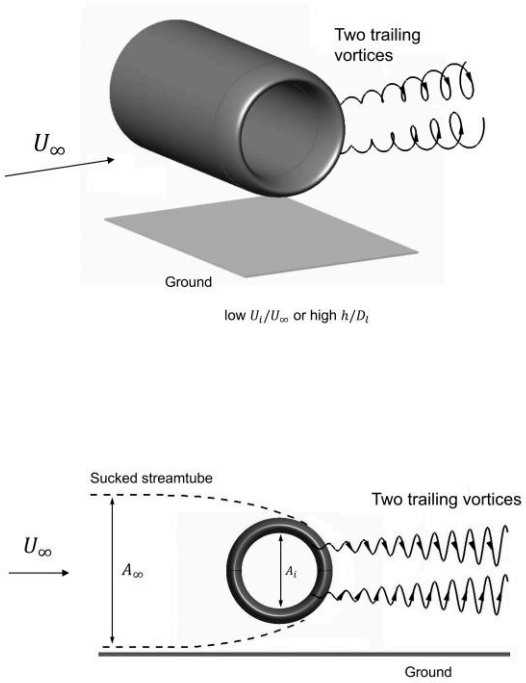

Figure 1: Flow field topology schematic under crosswind condition at high h/D_l where no ground vortex is present.

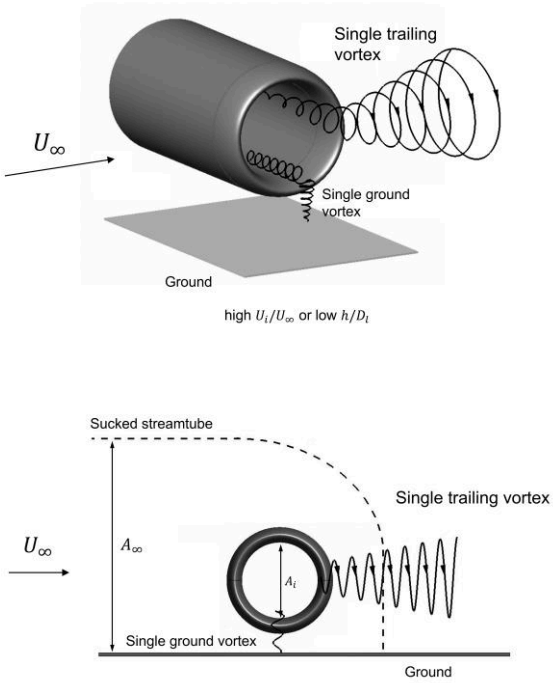

Figure 2: Flow field topology schematic under crosswind condition at low h/D_l with ground vortex.

The unsteady nature of the ground vortex in terms of variations of vortex core radius and position, defined as *vortex meandering* or *vortex wandering*, with respect to the crosswind velocity was also investigated experimentally by Wang and Gursul [10], also by means of Particle Image Velocimetry (PIV). Building on the experimental work by Murphy et al. [9], Rehby [11], Zantopp et al. [12], and Mishra et al. [13] performed CFD investigations of the aerodynamic of the ground vortex formation under crosswind by comparing steady-state numerical results with the experimental data obtained by Murphy's test campaign [7]. The characteristics of the ground vortex in terms of non-dimensional circulation $\Gamma^* = \Gamma/D_l U_i$ and the in-duct distortion in terms of total pressure distortion coefficient were calculated and compared with the experimental values, studying the effect of different parameter, that is non-dimensional height, freestream velocity, intake velocity, Reynolds number, and approaching boundary-layer, on these major features. The comparison of the computational results with the experimental data showed good similarities in terms of flow topology. In fact, the CFD methodology applied was able to capture the flow field under crosswind conditions for a variety of velocity ratios and ground clearance configurations. However, the CFD results seemed to overpredict the in-duct total pressure losses at low U_i/U_∞ (high crosswind velocity) and to underpredict the at high U_i/U_∞ (low crosswind velocity), while the vortex characteristics in terms of position, circulation, and radius presented slight mismatch with respect to the true values. Overall, the steady-state analysis performed, even if able to capture the main features of the flow, showed the limitations of such approach and the need of a transient approach to simulate such a flow.

More recently, Chen et al. [14] carried out an experimental and numerical study on the ground vortex field under crosswind analysing the vortex unsteadiness and instabilities in terms of intensity and frequency and identifying some variations of the ground vortex characteristics with velocity ratio. The simulations were carried out across a range of velocity ratios U^* for two fixed intake velocities at a fixed non-dimensional height, analysing the frequency of the ground vortex and validating against the experimental data available. The authors found out that, for the conditions investigated, the intensity of the ground vortex and its effect on the intake distortion unsteadily increase from a steady state up to a maximum and then decrease until the ground vortex is completely blown away with frequencies in the range of 10-20 Hz. Mendonca E Costa et al. [15] showed steady-state (RANS) and Hybrid (SAS Scale Adaptive Simulations) numerical simulations to provide a comprehensive characterization of vortex ingestion. The aim of the study was to develop a predictive model for vortex formation to be applied during experimental tests in a wind tunnel to track the vortex structures and to verify that the unsteady phenomena related to the vortex can be represented in a simplified computational domain without compromising the accuracy of the results. By comparing the unsteady simulations of ground vortex formation for two different configurations, one with an isolated intake and one with the same intake integrated in the wind-tunnel, the authors were able to live-track the vortex centre and to determine its radius along the course of the CFD simulations. However, no further analysis regarding the unsteady characteristics or the nature of intake flows under crosswind was provided, focusing only on the development of the methodology for vortex monitoring to be applied during the calculations. Many other CFD studies have been carried out to investigate the effect of crosswind on the performance of an aspirated inlet with ground plane ([16], [17]) or without ([18], [19]), or on the performance of the fan system in terms of stability and stall margin ([20]-[23]). However, the inherent unsteady characteristics of the ground vortex, when present, have not received much attention in previous works, hence its impact on the distortions at the Aerodynamic Interference Plane (AIP) is not fully understood.

The present study aims to assess the level of accuracy of CFD codes to predict ground vortex and to characterize the vortex unsteady behaviour and its effects on the intake performance across a range of free stream operating conditions. In the first part of the work the outcomes of RANS CFD simulations are validated against experimental data previously shown by Murphy [7] in terms of in-duct distortion and ground vortex characteristics. The aim of the CFD simulations was to determine the capability of RANS methods to predict the mean ground vortex and distortion characteristics and justify the necessity for higher fidelity CFD approaches such as URANS which is shown in the second part of the work. In fact, steady state CFD predictions may not be sufficiently representative of the flow physics, but it may still be pertinent to explore their capability to capture the time averaged characteristic of the ground vortex and fan face distortions due to the low computational cost that steady state simulations entail.

Most studies look at effects of steady forcing distortion on the blade and consider EO (engine order) excitation. In this work, it will be shown how the natural unsteadiness due to intake separation can cause NSV on fan blades.

2. EXPERIMENTAL APPARATUS AND METHODS

The experiments were conducted at Cranfield's $2.4\,m \times 1.8\,m$ low speed wind tunnel. A detailed description of the experimental setup is reported in [7]. The intake geometry was an axisymmetric cylindrical 1/30th scale model, with inner diameter $D_i = 0.10\,m$, highlight (or lip) diameter $D_l = 0.12\,m$, and a 2:1 lip aspect ratio (elliptical lip profile). A sketch of the intake is reported in Figure 3. The model did not include a spinner or a rotating fan (aspirated intake). A suction system provided a mass flow rate $\dot{m}$, through the intake of about $1.5\,kg/s$ corresponding to an intake Mach number M_i of 0.55, with a Reynolds number of 1.26×10^6 based on the intake inner diameter and average intake velocity U_i. Stereoscopic particle image velocimetry was used to measure the velocity components on a plane parallel to the ground at $h/D_l = 0.083$. A total pressure rake with 38 circumferential × 9 radial probes was used to measure the flow distortion at the AIP inside the duct, located at $0.7D_i$ from the highlight (see Figure 3). The distribution of the static pressure around the AIP was measured via 36 azimuthally equi-spaced static pressure taps located $0.65D_i$ downstream of

the duct's highlight plane. The geometrical parameters of the intake are summarized in Table 1.

The experimental dataset in [7] corresponding to a non-dimensional ground clearance equal to $h/D_l = 0.25$ was selected for the purpose of this paper. This set of data was deemed to be the most complete and representative for crosswind condition, because the ground vortex was present with increasing strength and the intake goes from fully attached to fully separated regime. The operating conditions and experimental results of interest from the test in terms of distortion coefficient DC_{60}, ground vortex non-dimensional circulation Γ^*, and non-dimensional vortex core radius r_c/r_i, are summarized in Table 2. The distortion coefficient DC_{60} is a measure of the loss in total pressure at a specified plane, defined as:

$$DC_{60} = \frac{P_{0,avg} - P_{0min,60}}{P_{0,avg} - P_{avg}} \quad (1)$$

where $P_{0min,60}$ is the lowest area-averaged total pressure in a sector of 60 deg angle at the AIP, $P_{0,avg}$ is the area-averaged total pressure at the AIP, and P_{avg} is the static pressure at the AIP.
The circulation Γ is related to the vorticity by the following relation

$$\Gamma = \int \omega_z dA \quad (2)$$

The circulation can be calculated by integrating the vorticity over circular areas with increasing radial distance from the vortex centre (see [7]).

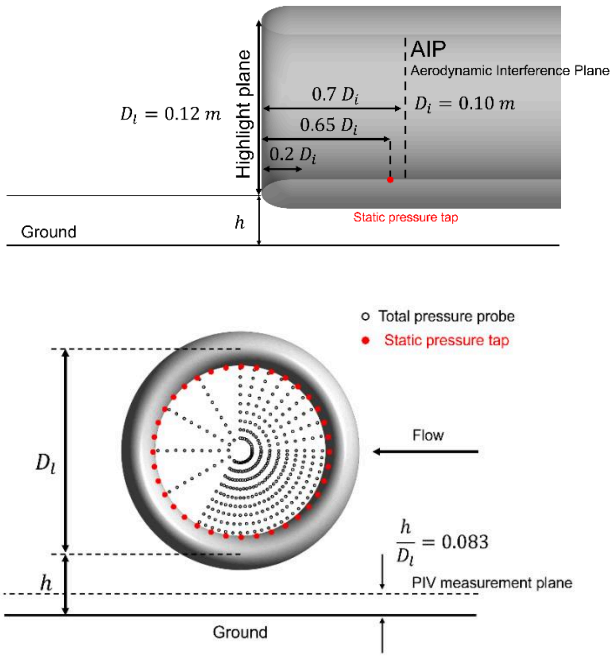

Figure 3: Intake geometry, ground plane, SPIV plane location and distortion rake definition (figures recreated based on [7]).

Table 1: Intake geometrical parameters.

Parameter		Value
Inner diameter, m	D_i	0.10
Highlight diameter, m	D_l	0.12
Maximum external diameter, m	D_{max}	0.14
Diameter ratio	D_{max}/D_i	1.4
Lip aspect ratio	AR	2

Table 2: Crosswind operating conditions and experimental mean vortex characteristics at the ground plane located at $h/D_l = 0.25$.

U^*	$U_\infty\ [m/s]$	DC_{60}	Γ^*	r_c/r_i
18.3	9.9	0.116	0.256	0.057
9.1	20.0	0.217	0.288	0.061
5.2	35.4	0.300	0.422	0.055

In Figure 4, the time averaged vortex core locations are shown with bars to indicate the standard deviation of the vortex core position and shapes to outline the envelope across which the vortex core was found over the 300 instantaneous SPIV snapshots [7], highlighting the unsteady behaviour of the ground vortex.

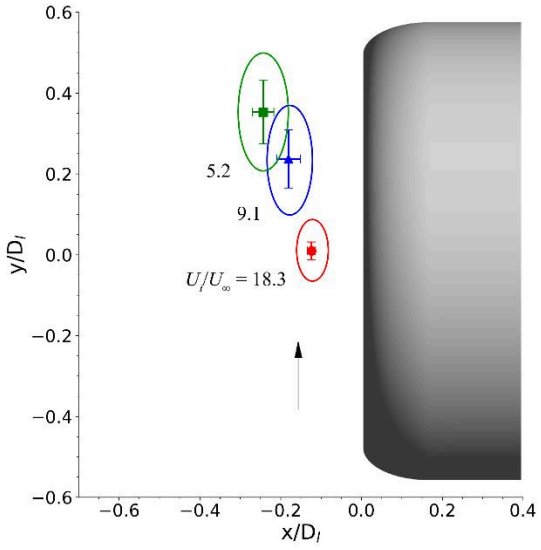

Figure 4: Averaged ground vortex core locations at the vortex measurement plane across the range of test conditions. Bars indicate the standard deviation in the x, y plane and the shapes indicate the extent of core movement over the unsteady SPIV dataset [7] (image redrawn with permission).

3. COMPUTATIONAL METHODS

The computational domain used to carry out all CFD simulations was a rectangular box with dimensions $25\ D_l \times 25\ D_l \times 12.5\ D_l$ in the x, y, and z directions respectively (see Figure 5). The intake duct was extended by approximately seven highlight diameters downstream to improve numerical stability of the model. Structured multi-block grids were generated using Cadence Pointwise v18.3R2 with multiple inflation layers with the nearest one to the wall at a non-dimensional distance of $y^+ \approx 1$ to capture viscous effects on the walls and accurately resolve the boundary layer around the intake surface and on the ground plane. To simulate the intake at crosswind conditions, the boundary conditions indicated in Figure 5 were applied at the various faces of the computational domain.

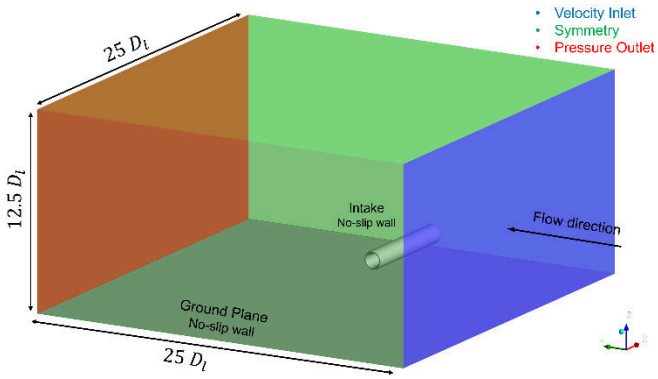

Figure 5: Computational domain and boundary conditions used for simulations.

The freestream turbulence was specified in terms of turbulent intensity and hydraulic diameter. A 3% turbulent intensity was assigned at the domain's inlet whereas a value of about 2 m was assumed for the hydraulic diameter, corresponding to the wind tunnel cross section. A non-uniform velocity profile approximated by the following expression

$$\frac{U(y)}{U_\infty} = \left(\frac{y}{0.104}\right)^{\frac{1}{8.28}} \tag{3}$$

was applied at the domain's inlet plane, in order to replicate the incoming boundary layer measured in the experiments and previously reported by Murphy in [7]. The CFD code ANSYS Fluent has been used for the RANS simulations. A density-based implicit formulation was used with a second-order upwind scheme for the spatial discretisation and a Green-Gauss node based gradient calculation. The k-ω SST turbulence model was used with curvature and low Reynolds number corrections and compressibility effects in place. To assess the influence of the grid resolution onto the outcomes of the simulations three grids were generated with 7.1, 17.2 and 41.1 million elements respectively. In each of the gird produced, the number of grid elements were changed in different sections of the intake duct, as shown in Figure 6 and Table 3, where (a) is the number of cells around the lip; (b), (c), (d), and (e) are the number of cells in the axial direction within the intake; (f) is the number of cells in the boundary layer normal to the wall; (g) is the number of cells in the radial direction from the boundary layer to the intake centreline; (h) is the number of cells around half circumference of the intake. Results from all three grids on ground vortex and AIP distortion characteristics are reported in Section 4 below as part of the RANS based simulations. For the URANS cases, the coarse grid with only 7.1M elements was used. The CFD code HADES was used for the unsteady computations due to its numerical efficiency. HADES solves the three-dimensional, viscous, and compressible RANS/URANS equations using a node-centred finite volume scheme with an edge-based data structure. Structured/Unstructured hybrid grids are compatible with the solver. The validations of the solver for a range of flows can be found in the previous works ([27], [28], and [29]). The time integration scheme is implicit and second order accurate. The time step for the URANS cases was chosen based on an iterative approach as the main frequencies of the unsteadiness were unknown. To determine an indicative characteristic timescale for the flow system, the convective time for a flow element to travel between the ground plane and the highlight plane was used. Unsteady simulations with finer grid resolution are currently in progress.

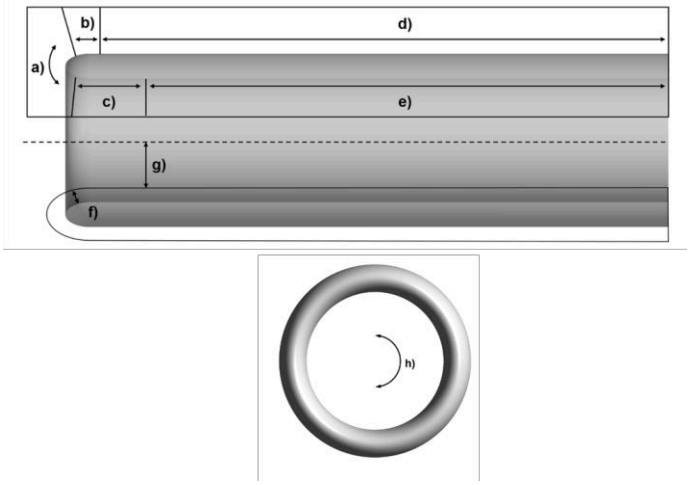

Figure 6: Grid blocks refined in the sensitivity analysis across the various parts of the intake duct. Grid blocks indicated in lower case letters.

Table 3: Mesh details of the sensitivity analysis. Lower case letters indicate grid blocks as defined in Figure 6.

	a)	b)	c)	d)	e)	f)	g)	h)
Coarse [7.1M]	25	35	35	99	119	30	25	69
Medium [17.2M]	37	49	49	109	129	30	35	101
Fine [41.1M]	55	67	67	119	153	30	49	153

4. RESULTS AND DISCUSSION

4.1 Steady state simulations

An initial grid sensitivity study between the three grids was carried out to determine the impact of the grid resolution on various properties of interest such as ground vortex properties, in-duct distortion properties and isentropic Mach number distributions along the intake's lip. However, the Grid Convergence Index between the three grids (GCI) was found acceptable for only a sub-set of the parameters of interest. This is attributed to the complex 3-dimensional nature of the flow that includes the presence of the ground vortex but more importantly the fact that this particularly flow field is in principle unsteady. As such, no selection of a single grid was made, and further flow field investigations were conducted with all three meshes.

The Intake Pressure Recovery, $IPR = P_{0,AIP}/P_{0,\infty}$, distributions across the AIP for each individual case across the range of non-dimensional crosswind flow velocities U* for the three computational grids is shown in Figure 7, while the predicted out-of-plane vorticity of the ground vortex is shown in Figure 8. In order to enable credible comparisons between the numerical and experimental data, the spatial resolution of the former was degraded to match the experimental resolution at both the ground vortex measurement plane as well as at the AIP. The CFD data reduction to calculate the pertinent ground vortex and AIP pressure recovery was carried out using the method described by Murphy in [7]. The original data from [7] are also shown below in Figure 7 and Figure 8 for comparison. As indicated by the numerical results across the range of U*, from low (U* = 18.3), to mild (U* = 9.1), to high (U* = 5.2) crosswind velocity, the grid spatial resolution influences very slightly the predicted total pressure loss at the AIP in terms of flow field topology inside the intake compared to the experiments. For the case at high crosswind (U* = 18.3) (see Figure 7 and Figure 8, top row), the fine grid with 41.1M elements indicates a roughly 50% narrower peak loss area at the AIP compared to the experimental data, showing a more defined vortex core with respect to the coarser grids, due to the higher density of elements on the plane. However, the depth of the loss appears to be under-estimated for all the grids. This under-prediction of the AIP total pressure loss characteristics is attributed to the under-prediction of the ground vortex non-dimensional vorticity which for the U* = 18.3 is shown in Figure 7, bottom row in comparison with the SPIV time averaged non-dimensional vorticity reported by Murphy in [7].

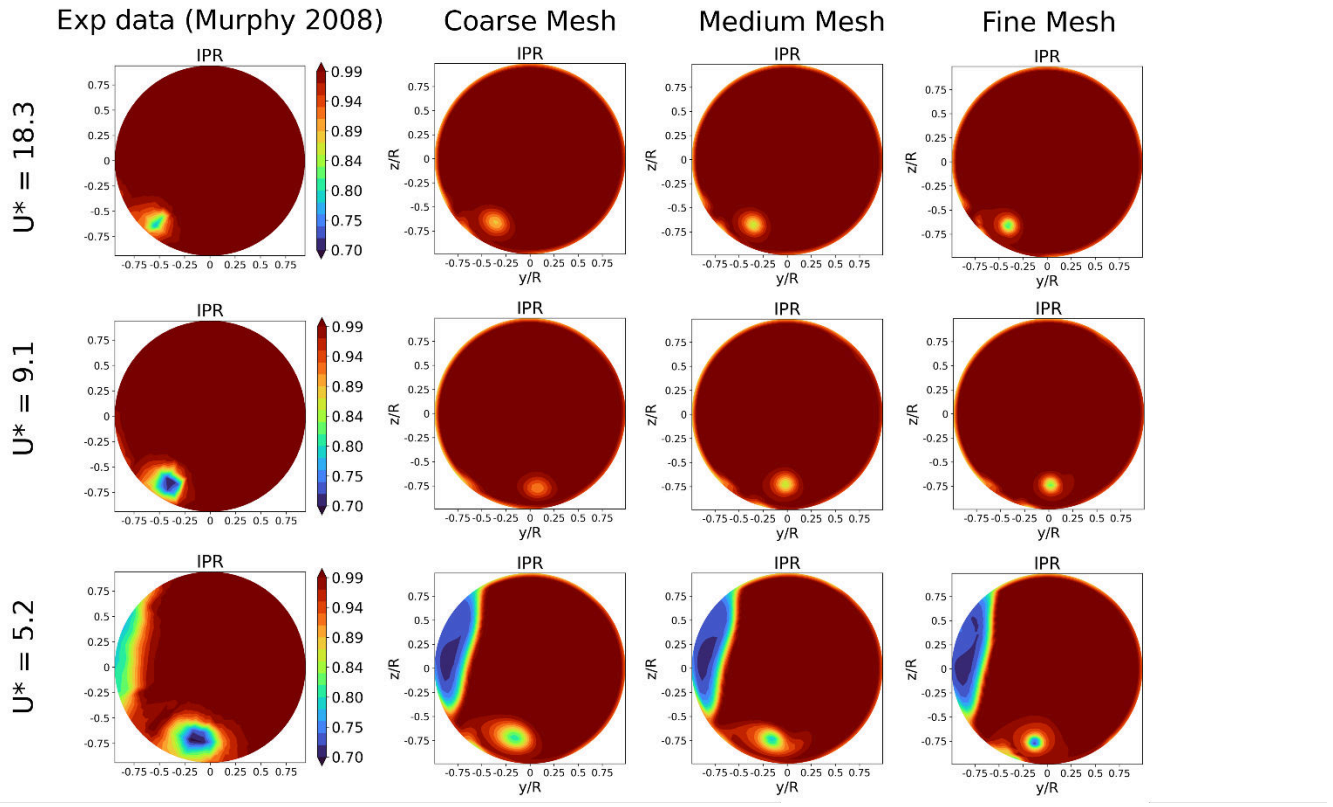

Figure 7: Total pressure recovery distribution at the AIP across the range of U* and grid resolutions. Top and bottom left images recreated using data from [7].

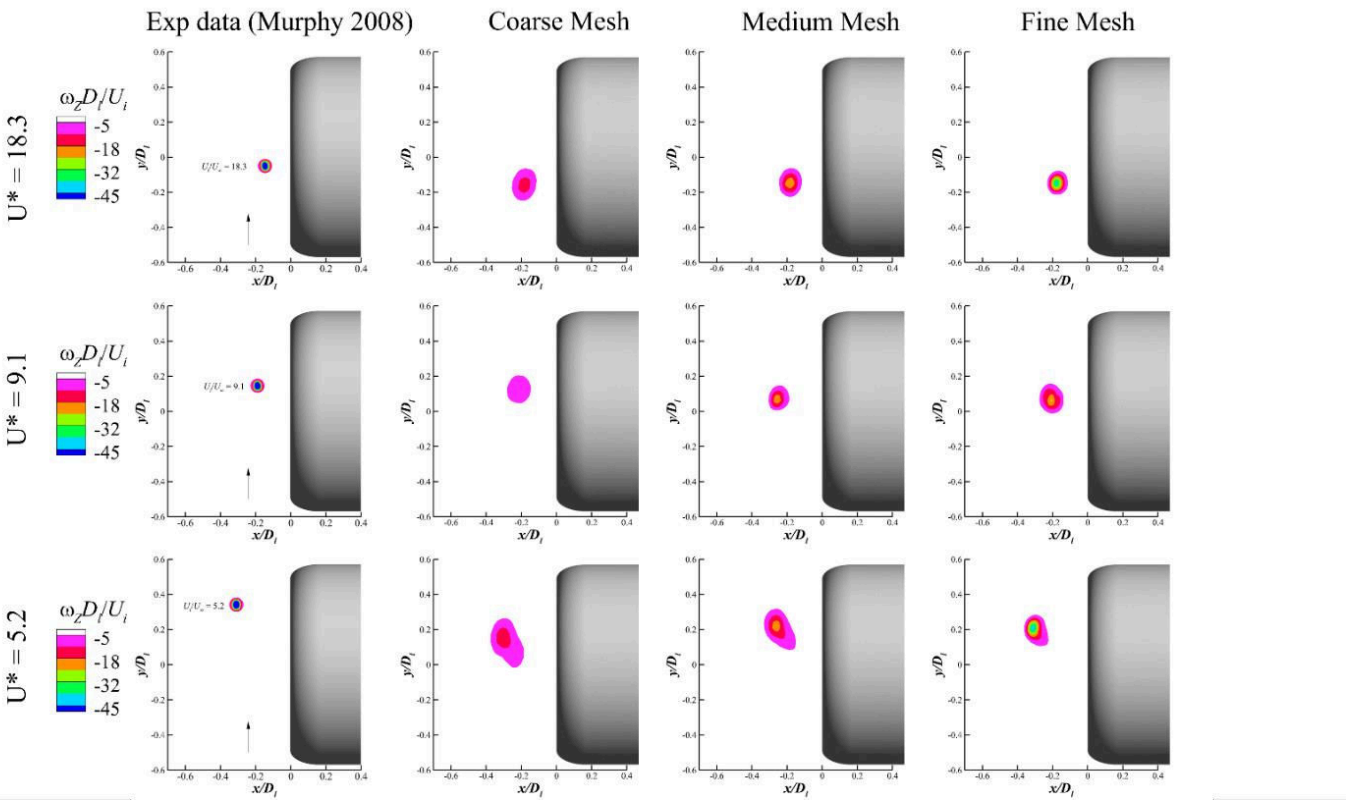

Figure 8: Out-of-plane vorticity at the ground plane across the range of U* and grid resolutions. Top and bottom left images recreated using data from [7].

The resolution of the grid influenced very little the location of the vortex core, while the radius of the vortex on the plane below the intake resulted to be between 4 and 2 times bigger than the experimental value across the range of grids, with a more defined prediction of the peak ground vortex vorticity for the fine mesh. Similar observations were made for the case at mild crosswind (U* = 9.1) which is shown in Figure 7 and Figure 8, central row, for the various grids in comparison with the experimental data on the left side of the image. As before, the substantial under-prediction of the AIP loss is linked with the under-prediction of the ground vortex peak vorticity which indicates that the numerical model tends to form a looser vortical structure at the ground plane compared to what was previously reported by Murphy [7]. This can be very significant when steady state RANS based simulations are employed for the prediction of the total pressure distortion profile within the intake duct because under-prediction of the peak loss but also of its extent across the plane may lead in under-estimation of the unsteady forces that a rotating fan blade experiences hence to produce a misleading evaluation of the blade's forced response Finally, for the cases at high crosswind (U* = 5.2) shown in Figure 7 and Figure 8, bottom row, apart from the notion of the ground vortex at the AIP, an additional inward flow separation is observed in both experimental and numerical results which causes substantially higher total pressure loss at the fan face plane. This loss due to the flow separation is substantially over-predicted by all numerical simulations compared to the experimental data. On the other hand, the loss due to the formation of the ground vortex was found substantially under-predicted by all CFD models in relation to the experimental data. The combination of the above two effects, resulted in a substantially inaccurate prediction of the overall total AIP pressure loss. This over-prediction of the total pressure losses may also influence the forced response predictions of a rotor under inlet flow distortion which in the case that higher loads are predicted, may result in the rotor being mechanically over-specified with potential penalties in the overall weight and other structural specifications of the fan system.

A summary of the total pressure predictions at the AIP in comparison to the experimental data for all three computational grids and across the range of U* cases is shown in Figure 9 at a fixed radial position passing through the peak loss region. These azimuthal distributions of the loss profile are useful to highlight the capability of the CFD to capture the position of the vortex and the depth of the loss around its core. The case at low crosswind velocity corresponding to U* = 18.3 showed perhaps the closest agreement with the experimental data in terms of azimuthal loss and position of the loss regime (Figure 9, top), even if the normalized radial position, r/R_{AIP}, and the circumferential position of the vortex differ roughly by 0.07 and

10 degrees, respectively. A similar observation is possibly valid for the case at high crosswind (U* = 5.2) but only for the losses related to the induction of the ground vortex which are shown to be in close agreement with previous experimental data. However, large discrepancies were observed on the prediction of the loss characteristics related to the flow separation for this case. The fine grid presents a more pronounced depth loss at the vortex centre that is closer to the experimental value, but a narrower vortex area compared to the experiments and the other grids. For the case at medium crosswind with U* = 9.1 both the total pressure loss as well as the position of the loss region were significantly under-predicted by all CFD simulations.

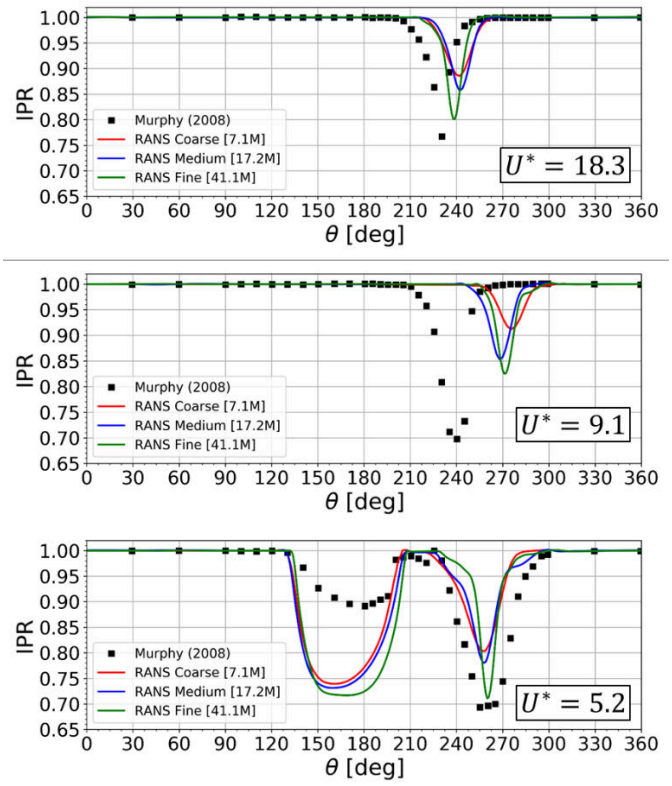

Figure 9: Numerical and experimental azimuthal loss distributions at a fixed radial position crossing the peak loss flow regime across the range of U* and grid resolutions. Experimental data points derived from Figure 7.

All the considerations above, can be quantified considering the numerical DC_{60} coefficient and the non-dimensional circulation Γ^* plotted against the measured value for the three cases and all computational grids in Figure 10 and Figure 11, respectively. Figure 10 clearly indicates the partially successful RANS capability to quantify the fan face loss and distortion linked to the induction of the ground vortex with or without flow separation in place. Although, predictions fall closer to the experimental data for the high U* case of 18.3, substantial discrepancies were shown for U* = 9.1 and U* = 5.2 where distortions were substantially under-predicted for the former and over-predicted for the latter due to the over-prediction of the separation related losses that were observed for U* = 5.2. For the case at low crosswind velocity (U* = 18.3), the discrepancy in the prediction of the DC_{60} distortion parameter from the measured data was found to be approximately 45% lower, while for the case at mild crosswind (U* = 9.1) the discrepancy was approximately 80%. For the case at high crosswind (U* = 5.2), the overall prediction of the DC_{60} distortion parameter at the fan face was found approximately 65% higher in relation to the experimental data.

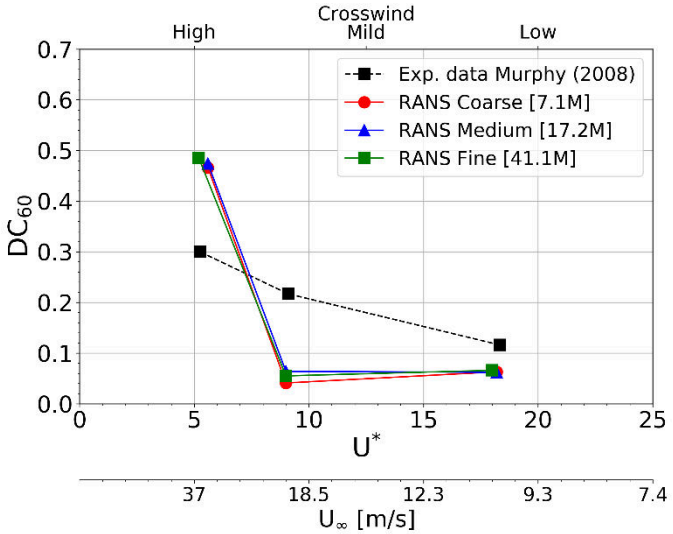

Figure 10: Fan face distortion across the range of U* for three computational grids and experimental data.

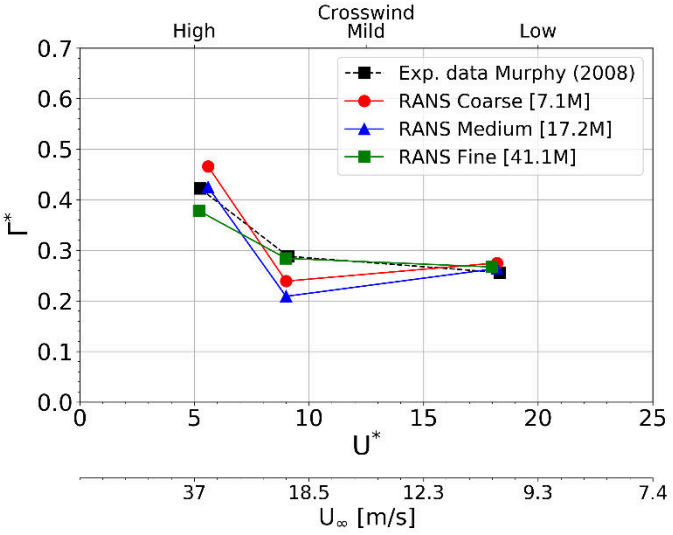

Figure 11: Ground vortex non-dimensional circulation across the range of U* for three computational grids and experimental data.

Based on the CFD outcomes from the RANS simulations in Figure 11, the non-dimensional vortex circulation is predicted within less than 16% of the experimental data with the predictions for U* = 5.2 being within 2% of the experimental observations. Nonetheless, a closer analysis of the numerical outputs shows that the although the non-dimensional vortex

circulation is predicted within a narrow margin in relation to the experimental data this is possibly an artifact of the vorticity predictions which are significantly under-predicted whereas the vortex radius is consistently over-estimated across the range of cases and grids (see Figure 8). To conclude, based on the above considerations, the grid resolution had a small influence on the prediction of the total pressure loss distortion coefficient and on the non-dimensional circulation of the vortex. In fact, even though the fine grid produced a higher and more defined vorticity peak loss on the plane below the intake and a higher total pressure loss at the vortex centre at the AIP, because of the increased mesh resolution on the planes, nearly no influence was observed among the grids on the prediction of the distortion parameters and on the vortex characteristics in terms of position and radius. The DC_{60} improvement between the three grids was 3.7% from coarse to medium and another 1.2% from medium to fine based on the DC_{60} Grid convergence index (GCI). The fine grid predictions showed a variation of the peak vorticity of approximately 50% in the vortex core compared to the experimental data, while the improvement on the predicted vortex circulation Γ^* was about 0.25% between the coarse and the medium grid and another 1.3% between the medium and the fine grid based on their Γ^* GCIs.

In conclusion, the overall evaluation of RANS based methods to predict the mean ground vortex and fan face distortion characteristics across a range of crosswind conditions indicated that the nature of the flow field is perhaps prohibitive of steady state methods as this may lead to inaccurate evaluations of the flow distortions at the fan face and possibly of the likelihood for the engine to ingest foreign debris with a chain of further consequences. The capability of the RANS methods could be further investigated by using a local mesh refinement at the AIP plane and on the ground plane in the correspondence of the location of the vortex and different turbulence models. However, a localized mesh refinement can cause an increase in the computational cost and in the complexity of the mesh topology and not necessarily correspond to a sufficient improvement of the accuracy of the solution, while eddy-viscosity turbulence models have been demonstrated to be inefficient in the prediction of crosswind flows around intakes, as stated in the introduction. This partial ability of the RANS methods to predict pressure loss puts the applicability of RANS approach for such flow predictions in doubt. As such, the necessity of unsteady methods of conventional or higher fidelity remains of key importance. Unsteady RANS simulations are shown in the following section of the current paper but methods of higher fidelity such as DES/DDES/IDDES or LES remain mostly unexplored.

4.2 Unsteady simulations

The measured data presented in Section 2 indicated unsteadiness on the ground plane during crosswind operation of the intake. The results also showed that the amplitude of unsteadiness increase with increasing crosswind speed (reducing U*). In this section unsteady CFD (URANS) is shown to ascertain the capabilities of URANS for modelling such flows by comparing against measured data. Thereafter, the impact of unsteadiness at the fan face is investigated. The trace of vortex core location on the ground plane is compared between CFD and measured data in Figure 12. To enable this comparison, the resolution of the CFD data was degraded to match the spatial resolution of the PIV plane used in the measurement. The CFD based location of vortex core is determined at the measurement as the CFD grid point with maximum out of plane vorticity magnitude. Figure 12 shows a similar trend between CFD and measured data although the envelope for the U*=5.2 was found to lie closer to the intake's centreline which doesn't agree with the experimental observations. Figure 12 also shows that the range of motion of the ground vortex in the CFD results is smaller than the measured data. This suggests that either URANS modelling fails to capture the vortex motion or that there are inaccuracies in interpolating the sparse measured data. Higher fidelity models (such as LES) will be required to identify the cause of this discrepancy.

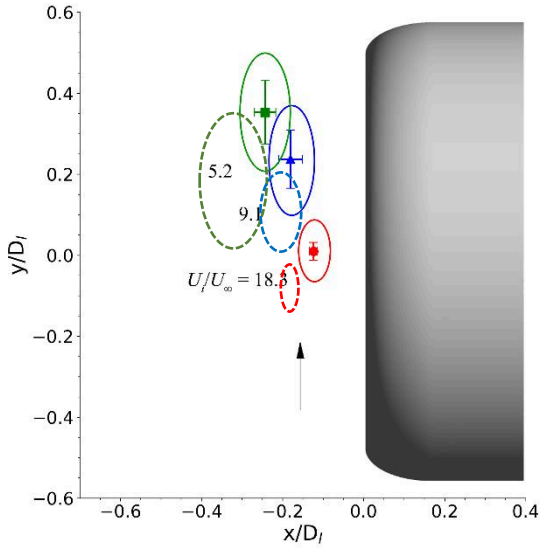

Figure 12: Comparison of CFD against measured data from [7] Dash lines denote CFD results (red indicates U* = 18.3; blue indicates a U* = 9.1; green indicates a U* = 5.2).

Figure 13 shows the contours of iso-surface Q criteria at four random instances for U* = 9.1 and U* = 5.2 (with $t_1 < t_2 < t_3 < t_4$). Time instants t_1 to t_4 have been chosen to show extreme events. In these figures the free stream flow comes from the right-hand side. It is seen that the ground vortex shows change in shape as well as position. It is also seen from this plot that for the case U* = 5.2 the ground vortex is at the edge of intake at T = t_3 and is not even present at T = t_4.

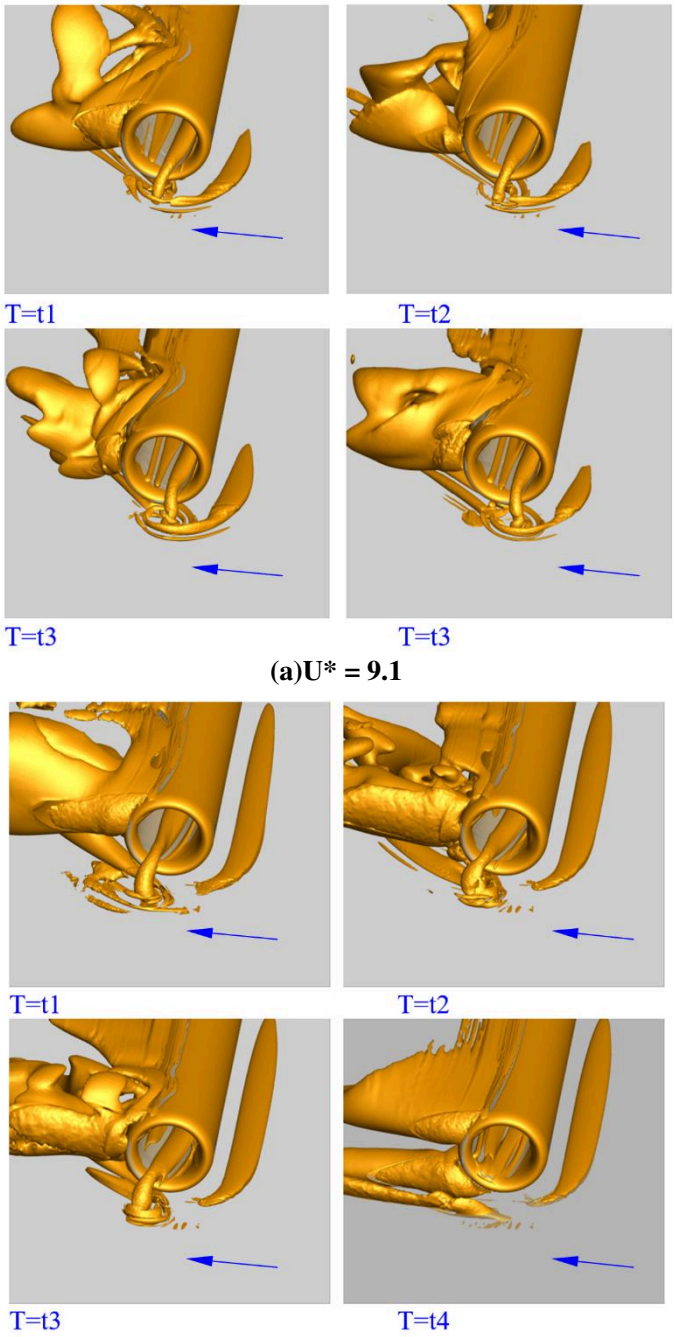

Figure 13: contours of Q criteria at 4 instant time for U* = 9.1 (a) and U* = 5.2 (b).

Next, the flow unsteadiness at the AIP is studied. The experimental data from [7] include no notion of unsteadiness at the AIP, hence this section relies exclusively on unsteady CFD results. Figure 14 shows the variations of total pressure at the fan face at four random instances of time for U* = 9.1. It is seen from these plots that for U* = 9.1 there is a significant circumferential motion in the position and amplitude of the vortex core (as defined by maximum pressure loss). The steady CFD results in Figure 9 showed a lower amplitude of total pressure loss at this condition. Figure 15 shows the variations of total pressure as a function of circumferential position (at a fixed radial position at 80% height) as four different instances of time. These results suggest that the discrepancies between CFD and measured data in Figure 9 is due to steady assumption in the computation. Figure 16 indicates that for U* = 5.2, there are two sources of unsteadiness at the AIP. The first is due to the ground vortex, and the second one is caused by the large, separated region at the lip which is also unsteady in nature. The distorted region due to flow separation at lip varies significantly in terms of position and size. The results in this section indicate that apart from usual CFD errors (grid density, turbulence model) steady flow assumption plays an important part in discrepancies between CFD and measured data which reinforces the previous conclusions about the applicability of RANS based methods for the prediction of the mean characteristics of these flows.

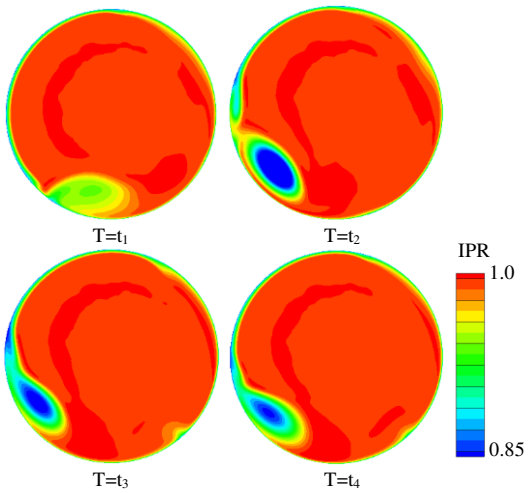

Figure 14: Variation of URANS total pressure at the AIP at four random instants of time for U* = 9.1.

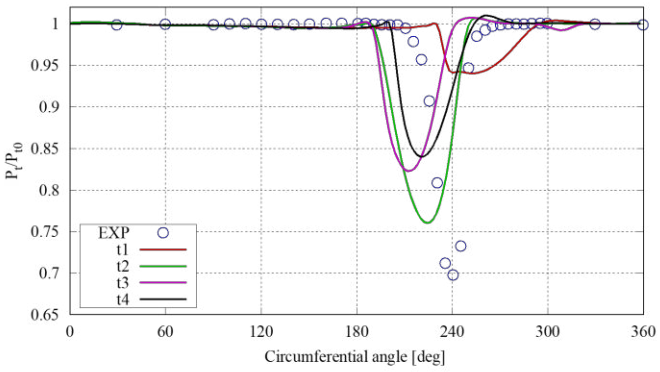

Figure 15: Instantaneous azimuthal loss distributions at a fixed radial position crossing the peak loss flow regime for velocity ratio U* = 9.1. Time averaged experimental data from [7] are shown for reference.

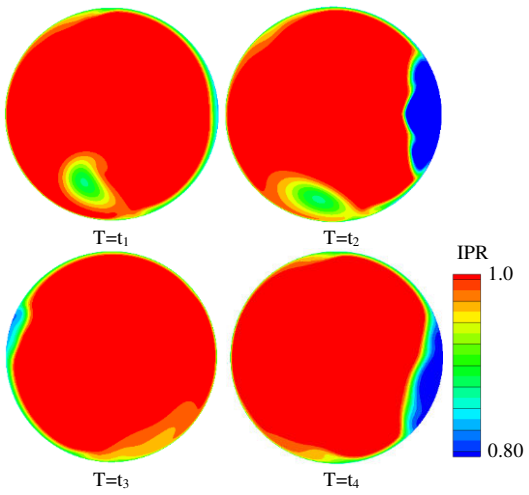

Figure 16: Variation of URANS total pressure at the AIP at four random instants of time for U* = 5.2.

4.3 Implications of unsteadiness on fan performance and vibration

In this section, the implications of unsteadiness in the intake on the fan aeroelastic and aerodynamic stability is discussed. For steady distortion (which is usually considered in forced response analysis of the fan due to inlet distortions) the fan will experience unsteady forcing at frequencies $F_N = N^* \Omega$ where N= 1,2,3 and Ω is the angular speed of the fan. In such situation the possibility of aeroelastic vibration can be identified by means of a Campbell diagram-based analysis. However, when the intake separation becomes unsteady (as shown in Figure 16) and has frequencies F_M (M=1,2,3,..), the fan will experience unsteady excitations at frequencies that can't be identified by Campbell diagram analysis as they represent non-synchronous frequencies defined as $F_{NM} = N \Omega + F_M$, N= 0,1,2…

Figure 17 shows an instantaneous distribution of circumferential angle at the AIP for the case with U*=9.1. Positive value of the circumferential angle denotes the traverse flow clockwise and the positive radial angle represents the flow outwards. It can be seen that apart from the unsteady total pressure distortions, the ground vortex will simultaneously result in large swirl distortion which varies with time. Such a swirl distortion can further degrade the performance of the blade as the incidence angle in front of the rotor deviates from the design value. It was also shown in [25] and [26] that, in presence of distortion, stall is initiated when the blade separation generated in the distorted region cannot be removed by the flow in the clean region. Figure 16 shows that unlike the work previously carried out in [25] and [26] for which fixed distortion planes were used, the location of distortion region moves circumferentially and radially as a function of time as depictured in Figure 16. Consequently, the stall characteristic of the blade becomes dependent of the unsteadiness.

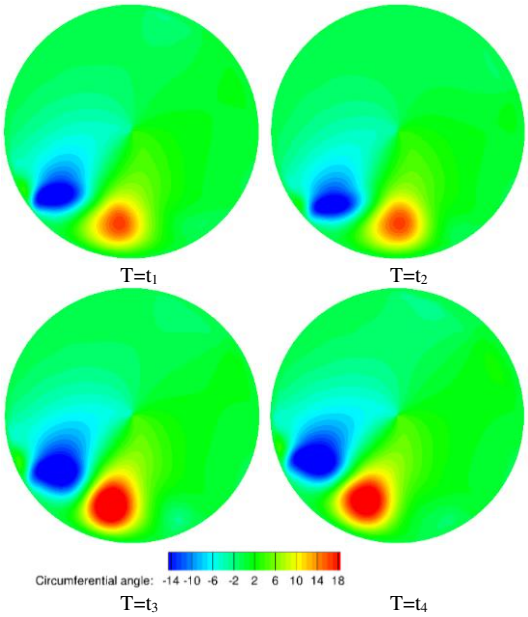

Figure 17: Instantaneous circumferential angle at the intake AIP for U* = 9.1

5. CONCLUSIONS

In this paper the flow characteristics of an aspirated intake at crosswind were investigated using RANS and URANS numerical simulations. Comparisons of the numerical results against experimental data obtained at the aerodynamic interface plane (AIP) of the intake duct indicated that a steady state simulation approach provides poor predictions the AIP mean flow distortion characteristics across the whole range of the examined non-dimensional crosswind speeds. This is more pronounced in the case where a significant part of the flow along the inner surface of the intake duct is separated, where the ability of RANS to generate the right amount of pressure loss in the zones of the flow influenced by the ground vortex and the inner lip separations was found very limited. Flow statistics from URANS computations could partially match the measure unsteady features on the ground plane. The analysis of the flow at the AIP showed significant unsteadiness linked with both the ground vortex and the lip separation. The results indicate that apart from usual CFD errors (due to grid density, turbulence model) steady flow assumption in computations plays an important role in discrepancies between CFD and measured data. In terms of fan operation, it is argued that apart from the synchronous vibrations caused by steady distortions, the unsteady distortions give rise to a new kind of non-synchronous vibration which is not usually accounted for in turbomachinery but can be detrimental to the stability of the fan, especially in the presence of extreme, instantaneous distortion events.

ACKNOWLEDGEMENTS

The authors would like to thank Rolls-Royce plc. and in particular Chris Sheaf and Daniel Gil-Prieto for supporting the work. This work was enabled through NIFTI project which has received funding from the Clean Sky 2 Joint Undertaking (JU) under Grant Agreement No 866521.

REFERENCES

[1] Rodert, L., and Garrett, F. Ingestion of Foreign Objects into Turbine Engines by Vortices

[2] Freeman, C., and Rowe, A. L. "Intake Engine Interactions of a Modern Large Turbofan Engine." Volume 1: Aircraft Engine; Marine; Turbomachinery; Microturbines and Small Turbomachinery, 1999. https://doi.org/10.1115/99-gt-344.

[3] Siervi, F. D., Viguier, H. C., Greitzer, E. M., and Tan, C. S. "Mechanisms of Inlet-Vortex Formation." Journal of Fluid Mechanics, Vol. 124, No. 1, 1982, p. 173. https://doi.org/10.1017/s0022112082002456.

[4] Shin, H. W., Greitzer, E. M., Cheng, W. K., Tan, C. S., and Shippee, C. L. "Circulation Measurements and Vortical Structure in an Inlet-Vortex Flow Field." Journal of Fluid Mechanics, Vol. 162, No. 1, 1986, pp. 463–487. https://doi.org/10.1017/s0022112086002124.

[5] Liu, W., Greitzer, E. M., and Tan, C. S. "Surface Static Pressures in an Inlet Vortex Flow Field." Journal of Engineering for Gas Turbines and Power, Vol. 107, No. 2, 1985, pp. 387–393. https://doi.org/10.1115/1.3239738.

[6] Brix, S., Neuwerth, G., and Jacob, D. "The Inlet-Vortex System of Jet Engines Operating near the Ground." 18th Applied Aerodynamics Conference, 2000. https://doi.org/10.2514/6.2000-3998.

[7] Murphy, J. "Intake Ground Vortex Aerodynamics." PhD thesis, Cranfield University, 2008 (full text available at: https://dspace.lib.cranfield.ac.uk/handle/1826/3515?show=full)

[8] Jia, W., Wu, Y., and Lei, Y. "Generation Mechanism and Aerodynamic Characteristic Modeling of Ground Vortex in Crosswind Condition." Aerospace Science and Technology, Vol. 99, 2020, p. 105581. https://doi.org/10.1016/j.ast.2019.105581.

[9] Murphy, J. P., and MacManus, D. G. "Ground Vortex Aerodynamics under Crosswind Conditions." Experiments in Fluids, Vol. 50, No. 1, 2010, pp. 109–124. https://doi.org/10.1007/s00348-010-0902-4.

[10] Wang, Z., and Gursul, I. "Unsteady Characteristics of Inlet Vortices." Experiments in Fluids, Vol. 53, No. 4, 2012, pp. 1015–1032. https://doi.org/10.1007/s00348-012-1340-2.

[11] Rehby, L. "Jet Engine Ground Vortex Studies." MSc thesis, Cranfield University, 2007.

[12] Zantopp S. "Jet Engine Ground Vortex Studies." MSc thesis, Cranfield University, 2008.

[13] Mishra, N., MacManus, D., and Murphy, J. "Intake Ground Vortex Characteristics." Proceedings of the Institution of Mechanical Engineers, Part G: Journal of Aerospace Engineering, Vol. 226, No. 11, 2011, pp. 1387–1400. https://doi.org/10.1177/0954410011424092.

[14] Chen, J., Wu, Y., Hua, O., and Wang, A. "Research on the Ground Vortex and Inlet Flow Field under the Ground Crosswind Condition." Aerospace Science and Technology, Vol. 115, 2021, p. 106772. https://doi.org/10.1016/j.ast.2021.106772.

[15] Mendonca E Costa, R., Millot, G., Raynal, S., Bouchet, J.-P., and Courtine, S. "Unsteady Simulation of Intake Ground Vortex Ingestion in Real Wind Tunnel Conditions." 55th 3AF International Conference on Applied Aerodynamics, 2000.

[16] Trapp, L. G., and Girardi, R. D. M. "Crosswind Effects on Engine Inlets: The Inlet Vortex." Journal of Aircraft, Vol. 47, No. 2, 2010, pp. 577–590. https://doi.org/10.2514/1.45743.

[17] Trapp, L. G., and Girardi, R. "Evaluation of Engine Inlet Vortices Using CFD." 50th AIAA Aerospace Sciences Meeting including the New Horizons Forum and Aerospace Exposition, 2012. https://doi.org/10.2514/6.2012-1200.

[18] Colin, Y., Aupoix, B., Boussuge, J.-F., and Chanez, P. "Numerical Simulation and Analysis of Crosswind Inlet Flows at Low Mach Numbers." 8th International Symposium on Experimental and Computational Aerothermodynamics of Internal Flows.

[19] Harjes, L., Bode, C., Grubert, J., Frantzheld, P., Koch, P., and Friedrichs, J. "Investigation of Jet Engine Intake Distortions Caused by Crosswind Conditions." Journal of the Global Power and Propulsion Society, Vol. 4, 2020, pp. 48–62. https://doi.org/10.33737/jgpps/118875.

[20] Mare, L. di, Simpson, G., and Sayma, A. I. "Fan Forced Response Due to Ground Vortex Ingestion." Volume 5: Marine; Microturbines and Small Turbomachinery; Oil and Gas Applications; Structures and Dynamics, Parts A and B, 2006, pp. 1123–1132. https://doi.org/10.1115/gt2006-90685.

[21] Green, J. S. "Forced Response of a Large Civil Fan Assembly." Volume 5: Structures and Dynamics, Parts A and B, 2008, pp. 685–692. https://doi.org/10.1115/gt2008-50319.

[22] Vunnam, K., and Hoover, R. "Modelling of Inlet Distortion Using a Combined Turbofan and Nacelle Inlet Model During Crosswind and Low Speed Forward Operation." Volume 1: Aircraft Engine; Ceramics; Coal, Biomass and Alternative Fuels; Wind Turbine Technology, 2011, pp. 371–380. https://doi.org/10.1115/gt2011-46466.

[23] Schnell, R., and Corroyer, J. "Coupled Fan and Intake Design Optimisation for Installed UHBR-engines with Ultra Short Nacelles." International Symposium of Air Breathing Engines, 2015 (full text available at: https://drc.libraries.uc.edu/handle/2374.UC/745656?show=full).

[24] Lee, K.-B., Wilson, M. J., and Vahdati, M. "Effects of Inlet Disturbances on Fan Stability." Journal of Engineering for Gas Turbines and Power, 2018. https://doi.org/10.1115/1.4042204.

[25] Zhang, W., and Vahdati, M. "A Parametric Study of The Effects of Inlet Distortion on Fan Aerodynamic Stability."

Journal of Turbomachinery, Vol. 141, No. 1, 2018. https://doi.org/10.1115/1.4041376.
[26] Fidalgo, V. J., Hall, C. A., and Colin, Y. “A Study of Fan-Distortion Interaction Within the NASA Rotor 67 Transonic Stage.” Journal of Turbomachinery, Vol. 134, No. 5, 2012, p. 051011. https://doi.org/10.1115/1.4003850.
[27] He, Xiao & Zhao, Fanzhou & Vahdati, Mehdi. “Evaluation of Spalart-Allmaras Turbulence Model Forms for a Transonic Axial Compressor”, 2020, 10.33737/gpps20-tc-13.
[28] He, X., Zhao, F., and Vahdati, M. "Detached Eddy Simulation: Recent Development and Application to Compressor Tip Leakage Flow." ASME. J. Turbomach. January 2022; 144(1): 011009. https://doi.org/10.1115/1.4052019
[29] He, X., Zhao, F., and Vahdati, M. "Uncertainty Quantification of Spalart–Allmaras Turbulence Model Coefficients for Compressor Stall." ASME. J. Turbomach. August 2021; 143(8): 081007. https://doi.org/10.1115/1.4050438